



Trans. Nonferrous Met. Soc. China 35(2025) 3383-3401

Transactions of Nonferrous Metals Society of China

www.tnmsc.cn



Microstructure, mechanical properties and corrosion behavior of Zr–2.5Nb alloy prepared by laser powder bed fusion

Yun-lei HUANG¹, Vyacheslav TROFIMOV¹, Feng LIU², Ming YAN^{3,4}, Jie ZHAN², Hui-xia LI⁵, Da ZENG⁶, Yong-qiang YANG¹, Chang-hui SONG¹

1. School of Mechanical and Automotive Engineering,

South China University of Technology, Guangzhou 510641, China;

2. Institute of Reactor Waste and Radiochemistry Research,

China Nuclear Power Technology Research Institute Co., Ltd., Shenzhen 518028, China;

- 3. Jiaxing Research Institute, Southern University of Science and Technology, Jiaxing 314031, China;
 - 4. Department of Interventional Radiology, The First Affiliated Hospital,

Southern University of Science and Technology, Shenzhen 518020, China;

- 5. Xi'an Sailong Metal Materials Co., Ltd., Xi'an 710016, China;
 - 6. Double Medical Technology Inc., Xiamen 361026, China

Received 7 February 2024; accepted 9 August 2024

Abstract: This study devoted to optimize the laser powder bed fusion (LPBF) parameters for the preparation of Zr-2.5Nb alloys, and was focused on power of incident laser beam and its scanning speed. The microstructure, mechanical and corrosion properties of samples prepared at different laser powers were investigated. The results show that high quality samples were obtained with the relative density over 99%, ultimate tensile strength of 980 MPa, and the elongation at fracture of 14.18%. At a scanning speed of 1400 mm/s, with increasing laser power from 120 to 180 W, two transformation processes: α' martensite coarsening and transition from an acicular into a zigzag structure $(\beta \rightarrow \alpha'/\alpha \rightarrow \alpha + \beta)$ occurred. Densification and α' martensite transition improved ductility and corrosion resistance at optimal value of the laser power while lower or higher laser power resulted in decreasing the ductility and corrosion resistance because of unfused particles and pores. Increasing β -Zr amount and size decreased the tensile strength due to the dislocation movement. Passive films, which were spontaneously formed at different laser powers, possessed an optimum corrosion resistance at the laser power of 160 W.

Key words: Zr-2.5Nb alloy; laser powder bed fusion; microstructure; mechanical properties; corrosion resistance

1 Introduction

Zirconium (Zr) and its alloys have been found widespread application in the nuclear, chemical, and biomedical fields due to their remarkable resistance to corrosion and irradiation, low absorption of the thermal neutrons, and excellent compatibility with the biological systems [1,2]. A

chemical element niobium (Nb) is known for its non-toxic and non-allergenic properties making it highly biocompatible [3]. Adding an appropriate amount (0.5–2.5 wt.%) of Nb to Zr alloys can improve its corrosion resistance and mechanical properties [4]. The Zr–2.5Nb alloy, with 2.5 wt.% Nb, holds a crucial significance as Zr-based alloy employed predominantly as a pressure tube material [5]. In recent years, Zr–2.5Nb alloy has attracted

considerable attention in the field of biomedical materials research for their potential applications in areas such as the hip and knee implants [6,7].

The manufacture of Zr-Nb alloy components by using traditional methods such as casting and forging possesses low efficiency and the material waste, potentially. They are not able to satisfy a production of complex customized structural components for industrial applications in a nuclear power and medicine. Laser powder bed fusion (LPBF), a type of additive manufacturing technology, melts laid metallic powders layer by layer to produce dense metallic components with personalized complex structures using a highenergy laser beam [8,9]. LPBF plays an important role in the biomedical field and a significant progress has been achieved in titanium (Ti) and its alloys [10,11]. Chemical elements of Zr and Ti belong to group IVB metallic elements in the periodic table and have similar physicochemical properties. However, LPBF is still in the beginning stage of the developing Zr alloys, and therefore it is necessary to study the feasibility of preparing Zr-2.5Nb alloys by using LPBF.

The high chemical activity of powdered zirconium alloys posed a significant problem for producing Zr alloy components using additive manufacturing [12]. Nevertheless, there are still cases of successfully producing Zr alloy by additive manufacturing. SONG et al [13] first successfully prepared nearly fully dense Zr-4 alloy using LPBF and observed fine acicular martensite in the microstructure significantly enhancing the strength of the Zr-4 alloy. YUE et al [14] employed selective laser melting to produce commercially pure zirconium (CP-Zr) components with an ultimate tensile strength of 746.3 MPa and an elongation of 27.1%. A significant presence of ultrafine α' martensite was distributed within the columnar prior β grains in the microstructure. The above studies show that the Zr alloy prepared by additive manufacturing can obtain improved spatial structure and better properties.

At present, the LPBF process is still in the beginning stage of developing Zr-2.5Nb alloy, and the effect and mechanism of LPBF process on the microstructure and properties of Zr-2.5Nb alloy need to be further understood. There is limited research on the phase composition and microstructural evolution that affect the mechanical

and corrosion resistance properties of the LPBF Zr–2.5Nb alloy. To address the above research gap, this research aims to reveal the regulation mechanism of the LPBF process on the phase composition and microstructure evolution of Zr–2.5Nb alloy, and further to reveal the mechanism of the laser parameters influence on the mechanical properties and corrosion resistance. The findings would provide guidance for preparing personalized and complex Zr–2.5Nb alloy components using additive manufacturing methods in the future, expanding the applications of the Zr–2.5Nb alloy.

2 Experimental

2.1 Material

Zr–2.5Nb alloy powder (Xi'an Sailong Metal Materials Co., Ltd., China) with a spherical particle shape and a particle size distribution of $15-45 \mu m$ was used for the experiments. The oxygen content was 0.12 wt.%. The powder morphology and the particle size distribution are shown in Figs. 1(a, b), and the chemical composition is given in Table 1.

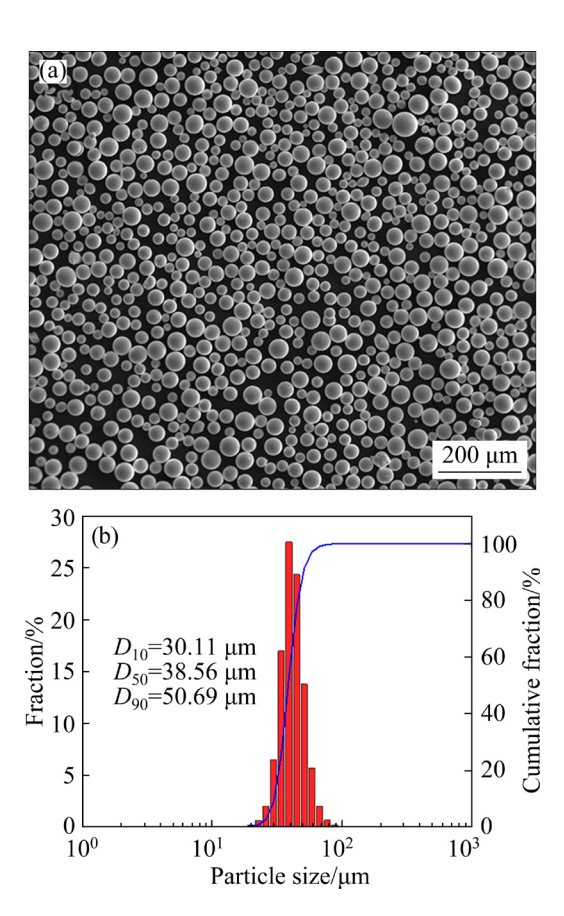


Fig. 1 Characterizations of Zr–2.5Nb alloy powder: (a) Powder morphology; (b) Particle size distribution

Table 1 Chemical composition of Zr–2.5Nb alloy powder (wt.%)

Zr	Nb	Cr	Fe	Hf	Sn
Bal.	2.53	0.0032	0.03	0.0024	0.0004

2.2 LPBF processes

The experimental equipment employed for printing Zr–2.5Nb alloy samples was the Dimetal–150 (Laseradd, Guangzhou, China), and the equipment is shown in Fig. 2(a). This equipment is equipped with a 500 W fiber laser and a high-precision scanning vibrator, ensuring precise and efficient printing. The equipment is gas-tight, ensuring that the forming chamber is in an oxygen-free environment during LPBF process, thus preventing combustion and oxidation of Zr–2.5Nb alloy powder and improving safety. Accounting for the high chemical activity of the Zr–2.5Nb alloy powder, the argon with a purity of 99.999% was used as a protective gas during the preparing process.

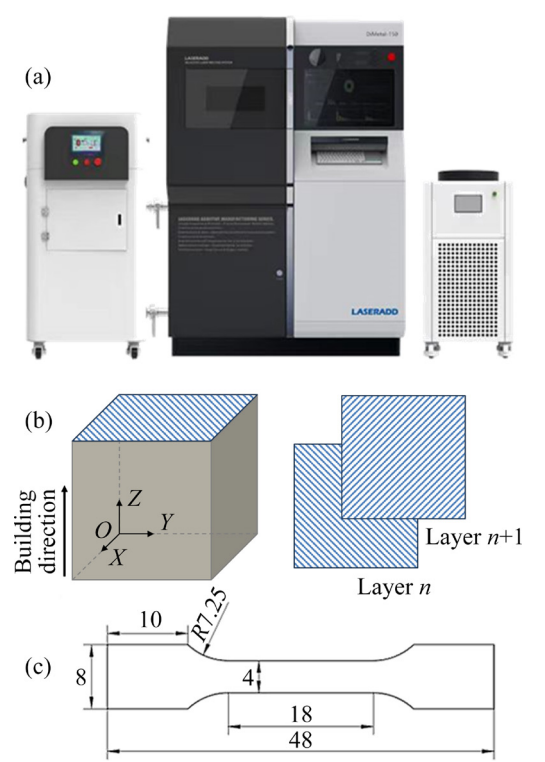


Fig. 2 Schematic of LPBF process: (a) Dimetal-150 equipment; (b) Schematic of orthogonal scanning strategy; (c) Dimension of tensile part (unit: mm)

The laser power of 120-180 W, scanning speed of 600-1800 mm/s, and hatch space of $70 \mu m$ were used for preliminary optimization. The layer thickness was set to be $30 \mu m$. The scanning

strategy chosen was orthogonal scanning, with a starting angle of 135° and an interlayer alternation angle of 90°, as shown in Fig. 2(b). The processing parameters used to prepare the Zr–2.5Nb alloy are summarized in Table 2. The dimensions of the tensile simples are shown in Fig. 2(c). A Ti6Al4V alloy substrate with dimensions of 150 mm × 150 mm × 25 mm was chosen. Before the experiment, the surface of the substrate was polished and smoothed, and the stains on the surface of the substrate were wiped off with anhydrous ethanol.

Table 2 Processing parameters used for LPBF Zr-2.5Nb alloy

Parameter	Value	
Laser power/W	120, 140, 160, 180	
Scanning speed/(mm·s ⁻¹)	600, 800, 1000, 1200, 1400, 1600	
Layer thickness/µm	30	
Laser beam diameter/µm	60-80	
Argon gas purity/%	≥99.999	
Delay period for laser on/μs	200	
Delay period for laser off/μs	350	

2.3 Characterization

The density of the cubic Zr-2.5Nb alloy was measured using the Archimedes method, which was repeated three times for each sample, and the relative density is calculated by the ratio of measured density to theoretical one. The XOZ planes of the cubic samples were chosen for micromorphology and microstructure characterization. After the surface of the samples was polished smoothly, the samples were etched using an etching reagent of 20 vol.% HF+45 vol.% HNO₃+35 vol.% H₂O. The morphology was observed under DMI-3000M optical microscope (OM) after wiping the sample surface for 25 s using a cotton swab. Since the surface of the Zr-2.5Nb alloy is prone to generating oxide film in air, which makes it not easy to be corroded, it is necessary to etch it in the etching solution for 60 s before a clear microstructure can be observed in a FEI QUANTA 250 scanning electron microscope (SEM). The phase identification was carried out by Malvern Panalytical X-ray diffraction (XRD) in the 2θ range from 20° to 90° at a scan rate of 12 (°)/min with a scan step of 0.013°. The samples were polished

with argon ions using an ion-thinning instrument (Fischione 1051, America), and the electron backscattered diffraction (EBSD) data were collected using a thermal field emission scanning electron microscope (FEI Verios 5 UC, America) operating at 20 kV with a scanning step of 0.12 μ m. The transmission electron microscope (TEM) characterization was performed on a field emission transmission electron microscope (FEI Talos F200S TEM, Thermo Fisher Scientific, USA).

2.4 Mechanical testing

The microhardness was tested with a Vickers microhardness tester (DHV-1000Z, China) with a load of 200 g and a dwell time of 15 s. The microhardness was measured at five different positions, and the average value was calculated for each sample. The tensile properties of the specimens were measured by a universal testing machine (SUST CMT5504, China) at room temperature with three specimens in each group. The ultimate tensile strength and elongation were determined by a 10/7 extensometer, with the tensile rate set at 0.5 mm/min. The fracture morphology was observed by scanning electron microscopy (Zeiss Merlin, Germany).

2.5 Electrochemical corrosion measurement

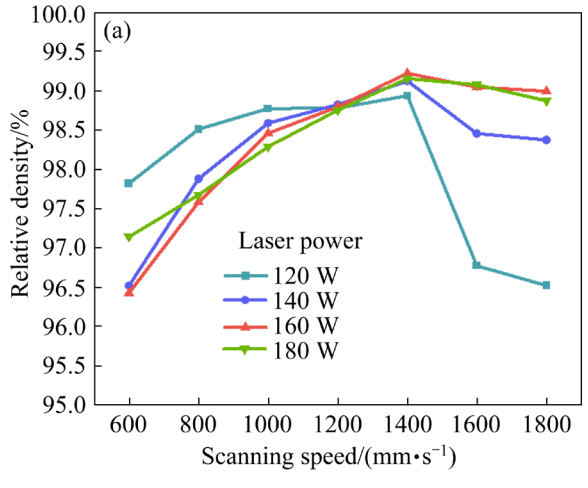
Electrochemical experiments were performed using a CHI604e electrochemical workstation with a three-electrode system consisting of a counter electrode Pt (thin sheet), a reference electrode (Ag/AgCl electrode), and a working electrode (sample). The working electrolyte was 3.5 wt.% NaCl solution. The samples were polished until there were no scratches before the experiment.

To ensure that the passive film on the sample surface was in a dynamically stable state, the sample was subjected to open circuit potential (OCP) measurements for 5400 s. Electrochemical impedance spectroscopy (EIS) measurements were conducted under OCP conditions using a sinusoidal potential perturbation of 10 mV. The frequency sweep ranged from 0.01 Hz to 100000 Hz. The impedance data were analyzed and fitted to the corresponding equivalent electrical circuit using Zview software. The potentiodynamic polarization measurement was conducted with a scan rate of 1 mV/s in the range from -1.0 V to 2.0 V (vs Ag/AgCl).

3 Results and discussion

3.1 Relative density

Figure 3 demonstrates the relative density of the Zr–2.5Nb alloy prepared with different laser powers and scanning speeds. Based on the data presented in Fig. 3(a), it can be observed that the relative density of the Zr–2.5Nb alloy displayed an initial increase and subsequent decrease trend with increasing scanning speed and varying laser powers. The peak relative density was achieved at a scanning speed of 1400 mm/s. Measurement of the actual density of the Zr–2.5Nb alloy using the Archimedes drainage method found that the relative densities of the Zr–2.5Nb alloy were more than 98% at a scanning speed of 1400 mm/s, and the relative densities reached a maximum of 99.22% at a laser power of 160 W, as shown in Fig. 3(b).



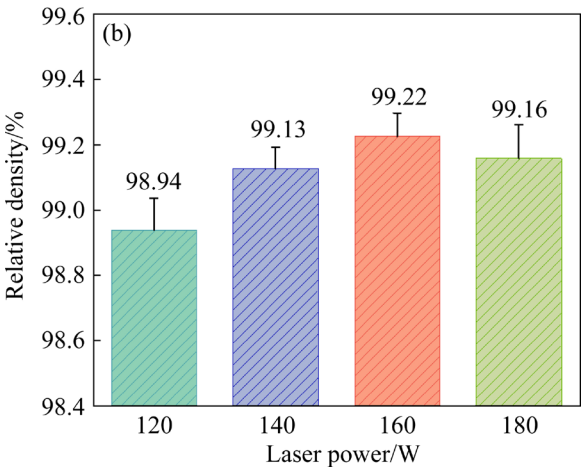


Fig. 3 Relative density of Zr–2.5Nb alloy prepared by LPBF: (a) Line chart of relative density varying with laser power and scanning speed; (b) Histogram of relative density varying with laser power at scanning speed of 1400 mm/s

The macroscopic morphology of the Zr-2.5Nb alloy with different laser powers and scanning speeds was observed using an optical microscope, as shown in Fig. 4. The content of internal pores of the sample decreased first and then increased as the scanning speed increased, similar to the evolution of relative density. To perform a more detailed analysis of the pores, samples at different scanning speeds were chosen for magnification, as shown in Fig. 4. At low scanning speeds (Samples 4, 7 and 10), most of the pores in the sample were subrounded. As the scanning speed increased, the number of pores gradually decreased and the pore aperture gradually decreased from 99.246 to 16.643 µm. When the scanning speed was 1400 mm/s (Sample 19), there were almost no pores formed inside the sample, indicating good bonding between layers. Therefore, the relative density of the Zr-2.5Nb alloy was the highest at a scanning speed of 1400 mm/s. If the scanning speed was increased up to 1600 mm/s, the number of pores began to increase again. However, unlike the pores at low scanning speeds, the pores at high scanning speed exhibited irregular shapes.

The evolution of pores is mainly depended on the incident laser energy. The laser energy density (E) is calculated from Eq. (1) [15]:

$$E=P/(v\cdot t\cdot h) \tag{1}$$

where P is the laser power, v is the scanning speed, t is the layer thickness, and h is the hatch spacing. From Eq. (1), the lower the scanning speed, the higher the laser energy density. An evolution of relative density of a sample with changing the laser energy density is shown in Fig. 5. Combined with Fig. 4, it can be seen that if the laser beam energy was low, the powder particles at the laser beam edge obtained insufficient laser energy, and then some unfused spherical powder and irregular pores appeared at the bottom of the molten pool. If the laser beam energy was too high, the width and depth of the molten pool increased. If the laser beam energy density exceeded a certain threshold, then the keyholes were formed inside the molten pool [16,17]. The hydrostatic pressure, acting on the sides of the keyholes, aimed to decrease the surface area of the pores, causing them to assume a subrounded shape eventually [18,19].

3.2 Microstructure and composition

Figure 6 presents XRD patterns of Zr–2.5Nb alloy samples prepared by LPBF with laser powers of 120–180 W. Under room temperature conditions, Zr–2.5Nb alloy typically consisted of α -Zr phase

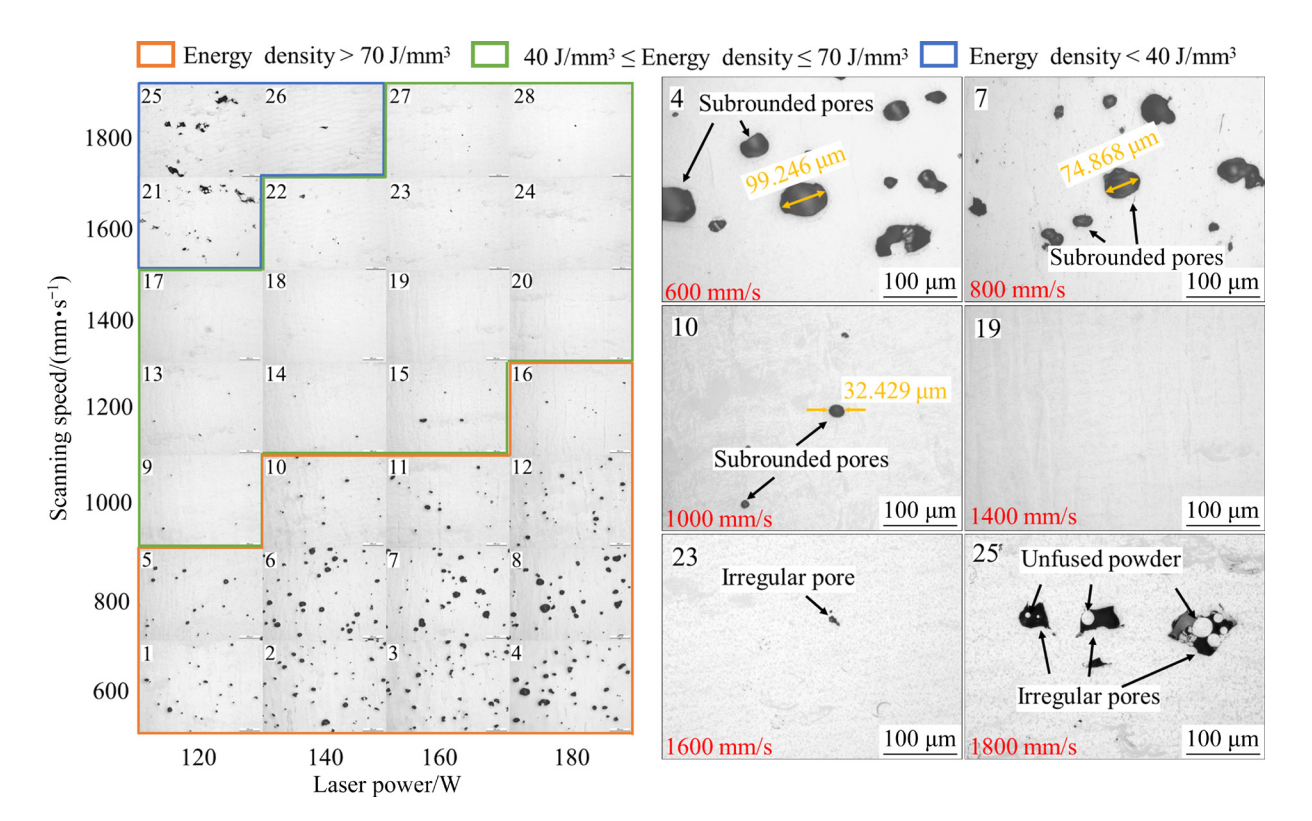


Fig. 4 Optical morphologies of Zr-2.5Nb alloy with different laser powers and scanning speeds

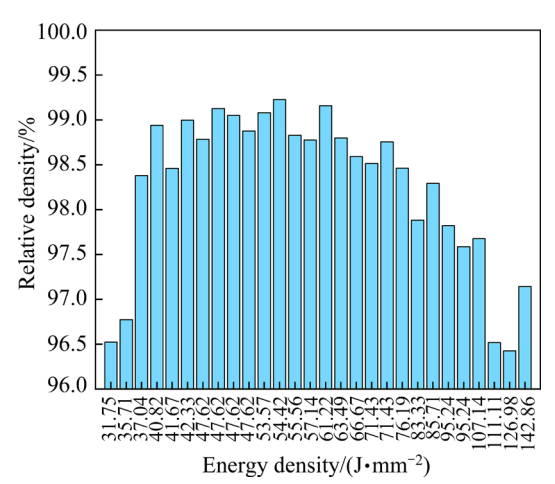


Fig. 5 Variation of relative density of Zr-2.5Nb alloy with laser energy density

and metastable β -Zr phase, with Nb mainly existing in the β -Zr phase (around 20 wt.% Nb in β -Zr) [20]. Diffraction peaks of the α -Zr appeared in all samples, and no obvious β -Zr phase diffraction peaks appeared. This is due to the fact that the β phase concentration is less than the detection threshold of XRD (volume fraction <1%) [21]. The detailed scanning results for the sample in the 2θ range of 34° - 38° are shown in Fig. 6(c). The standard angles (34.828° and 36.510°), corresponding to the (002) and (101) of α -Zr phases in accordance to PDF# 89-3045, are indicated by the black dashed lines. It can be found that with the laser power increasing, the diffraction peaks of the α phase gradually shifted towards lower angles.

According to Bragg's rule for the diffraction angles $(2d\sin\theta=n\lambda)$, the decrease of the 2θ angle leads to an increase in the lattice plane distance, d. This indicated that laser-induced non-equilibrium metallurgical process caused lattice distortion in

the α -Zr matrix. Meanwhile, the relative intensities of the diffraction peaks under different laser powers are significantly differed. As the laser power increased, the intensities of (002) and (101) peaks showed a trend of first increasing and then decreasing, and (100) peak showed irregular changes, as shown in Fig. 6(b). Thus, an obvious evolution of the crystal structure occurred with the increase of laser energy input.

Figure 7 shows the OM morphology of the Zr-2.5Nb alloy samples prepared by LPBF with laser power of 120-180 W. In the morphology of all samples, there were columnar prior β grains that grew along the building direction (i.e., the Z direction). Within the prior β columnar grain, a crisscross pattern of acicular martensitic phases, known as α' martensite, existed. At a relatively low laser power (120 W), the contour of the prior β column was not distinct, and the precipitation of the α' martensite phase was minimal. As the laser power increased gradually, the boundary of the β grain became more notable. The prior β columnar grain exhibited an average width that was approximately equal to the scanning spacing of 70 µm, while its average length extended up to 3 mm.

More detailed microstructure characteristics of the LPBF Zr-2.5Nb alloy at laser power of 120-180 W are shown in Fig. 8. It can be observed that the α' martensite was generally irregularly distributed, and the formation of martensitic needles was limited by the prior β grain boundary. At lower laser power, the precipitation of α' martensite was not pronounced, as shown in Figs. 8(a, b). When the laser power was 140 W, it could be noticed that parallel acicular clusters of the α' martensite were

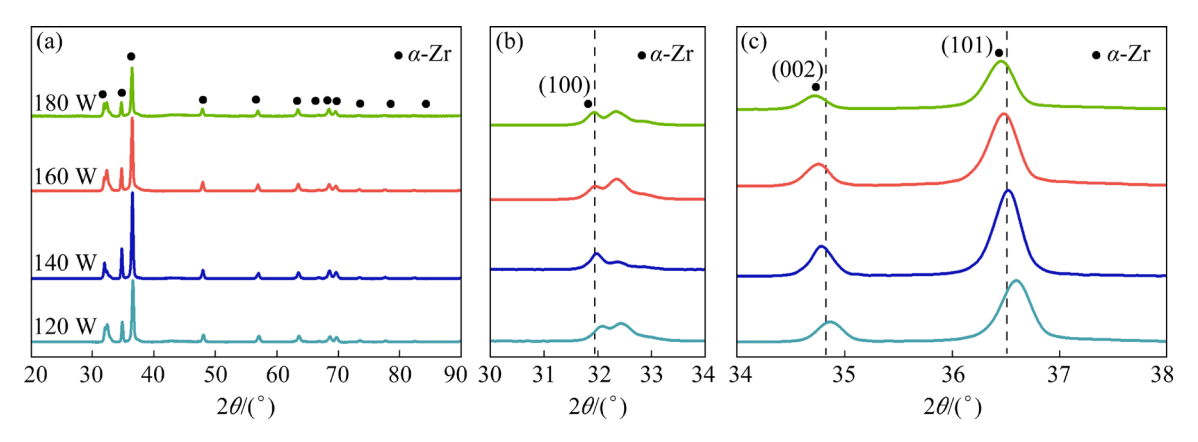


Fig. 6 XRD patterns of LPBF Zr–2.5Nb alloy samples with different laser powers: (a) Scanning from 20° to 90°; (b) Scanning from 30° to 34°; (c) Scanning from 34° to 38°

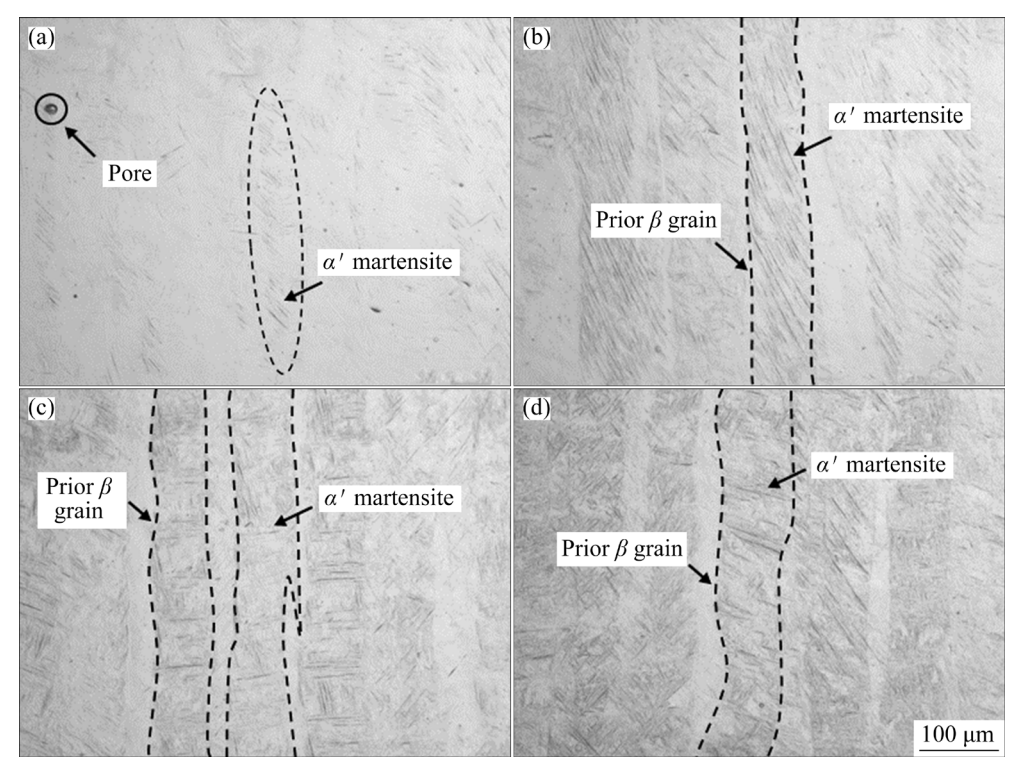


Fig. 7 OM morphologies of Zr–2.5Nb alloy samples prepared by LPBF at different laser powers: (a) 120 W; (b) 140 W; (c) 160 W; (d) 180 W

formed. The acicular phases were arranged at approximately $\pm 45^{\circ}$ with respect to the alignment of β columnar crystals, as shown in Figs. 8(c, d). According to Refs. [14,22], the growth direction of α' martensite is mainly due to the special Burgers relationship between α/α' phases and β phase. If the laser power was equal to 160 W, then the crystal structure of the α' martensite phase further grew. The length of the majority of the acicular martensitic phases was less than 15 μ m and their width was less than 1.5 μ m. As the laser power was increased to 180 W, the acicular martensitic phases gradually transformed into a zigzag shape, and the boundary of the columnar β crystals became increasingly blurred, as shown in Figs. 8(e, h).

The EBSD results of the Zr–2.5Nb alloy prepared at laser power of 140 and 160 W are shown in Fig. 9. Figures 9(b, d) display the texture and grain morphology of the Zr–2.5Nb alloy, where grains aligning in same direction typically exhibited the same crystal orientation (color). Figure 9(a) clearly demonstrated that the initial β grains exhibited growth along the building direction, while the acicular α' martensite phase grew along the original β grain boundaries. This observation was consistent with the findings obtained through OM

and SEM. The phase constitution shown in Figs. 9(b, e) revealed that the β -Zr (the red area) exhibited an irregular distribution in the sample, with a volume fraction of only about 0.07% in the sample prepared at 140 W. In contrast, its volume fraction increased to 0.2% in the sample prepared at 160 W, indicating that the higher laser power accelerated the transition of $\alpha' \rightarrow \alpha + \beta$. The grain size distribution, as shown in Figs. 9(c, f), was determined using the short axis length obtained through grain fitting. As the laser power was increased from 140 to 160 W, the average grain size increases from 1.4 to 1.57 µm.

Figures 10(a–d) show the pole figures of the α -Zr phase and the β -Zr phase of the Zr–2.5Nb alloy. With increasing laser power from 140 to 160 W, the maximum texture index of α -Zr increased from 18.62 to 24.27, and the maximum texture index of β -Zr increased from 21.59 to 27.75. Thus, increasing laser power significantly increased the orientation of the α -Zr grains and the β -Zr grains. The transition between the α/α' phases and the β phase of zirconium typically conforms to the Burgers orientation relationship ($\{0001\}_{\alpha}//\{110\}_{\beta}$ and $\langle 11\overline{20}\rangle_{\alpha}//\langle 111\rangle_{\beta}$), which encompasses a total of 12 variants [20,23]. Out of the 132 potential

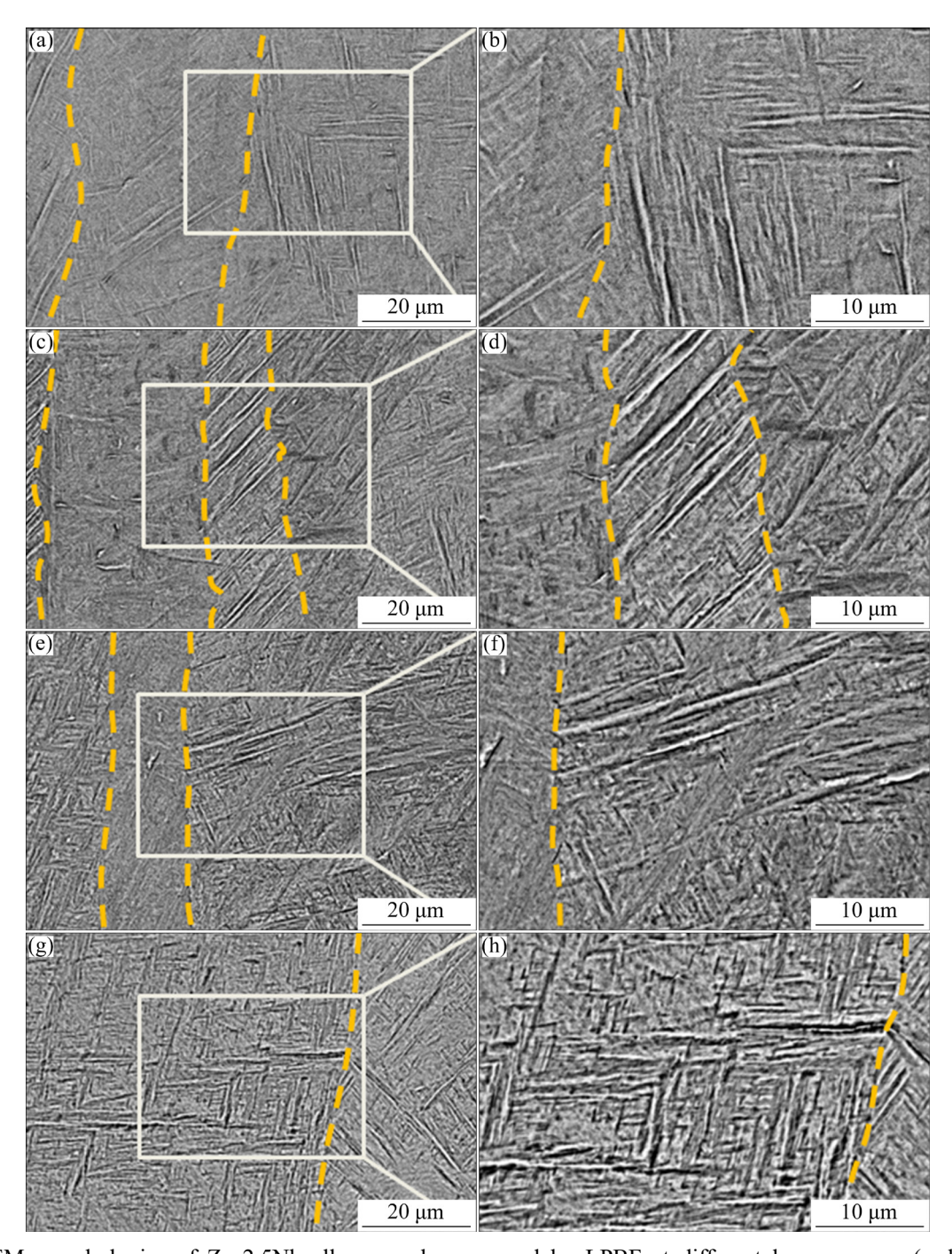


Fig. 8 SEM morphologies of Zr-2.5Nb alloy samples prepared by LPBF at different laser powers: (a, b) 120 W; (c, d) 140 W; (e, f) 160 W; (g, h) 180 W

combinations derived from these 12 variants, only 5 distinct misorientations exist, approximately taking place at 10.5° , 60° , 60.8° , 63.3° , and 90° [23]. By observing Figs. 10(e, f), it became apparent that the misorientation angles among α' martensite grains were predominantly within the range of $60^{\circ}-63.3^{\circ}$, and with a few instances at 90° . This phenomenon is similar to that obtained by CHAI et al [24] in a study of quenched Zr alloy. Due to

complex dynamic thermal cycle and rapid cooling characteristics during the LPBF process, acicular α' martensite transforms from the metastable original β grains. Combined with the analysis of the phase constitution, it could be concluded that increasing the laser power caused the transition of $\beta \rightarrow \alpha'/\alpha \rightarrow \alpha + \beta$ to occur in the Zr-2.5Nb alloy.

To reveal the internal characteristics of the Zr-2.5Nb alloy more clearly, the TEM was used for

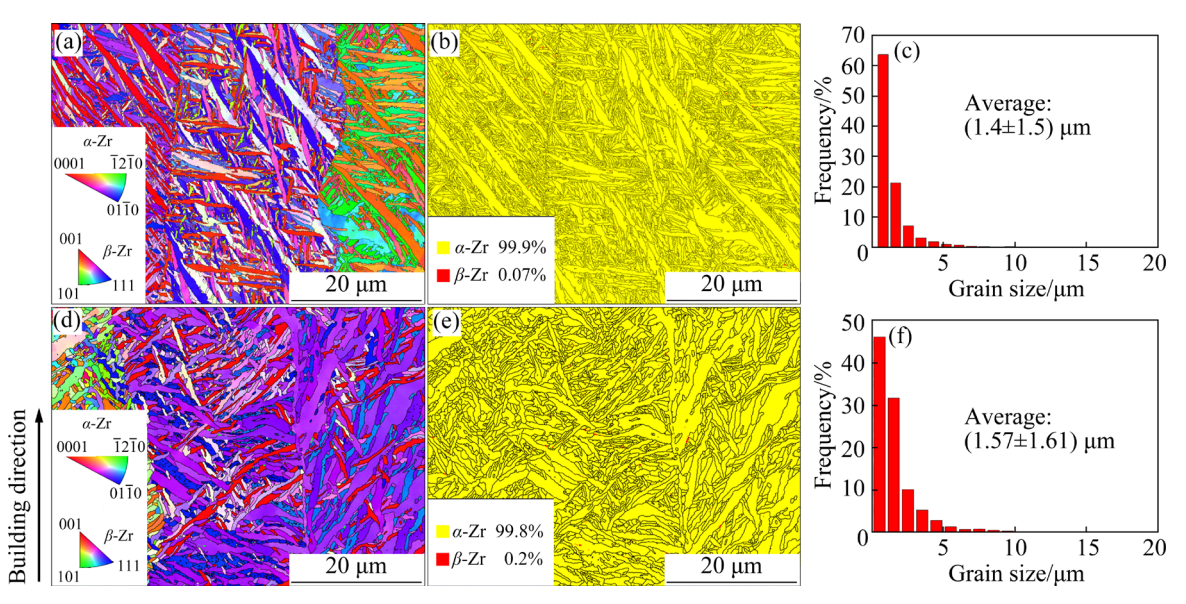


Fig. 9 EBSD results of Zr-2.5Nb alloy prepared by LPBF at different laser powers: (a-c) IPF map, phase constitution, and grain size of sample prepared at laser power of 140 W; (d-f) IPF map, phase constitution, and grain size of sample prepared at laser power of 160 W

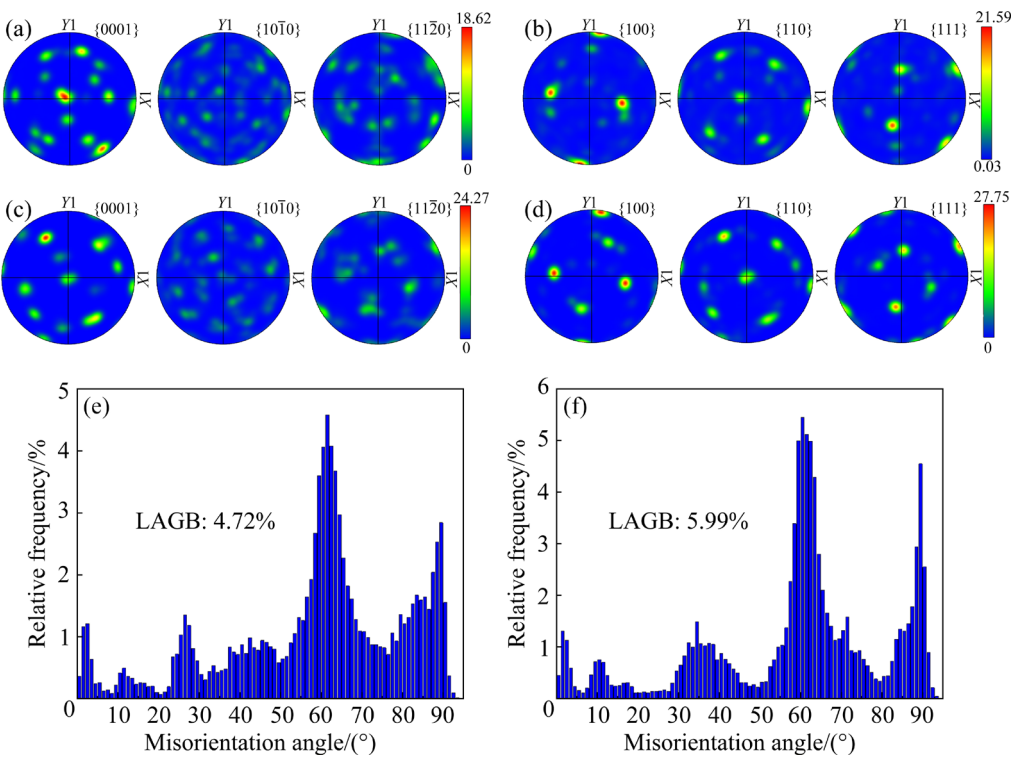


Fig. 10 Pole figures of α-Zr (a, c) and β-Zr (b, d), and misorientation angle (e, f) of Zr–2.5Nb alloy prepared by LPBF at different laser powers: (a, b, e) 140 W; (c, d, f) 160 W

analysis of the Zr–2.5Nb sample prepared by LPBF with a power of 160 W, as shown in Fig. 11. The evident twin martensite could be seen from the bright filed (BF) image in Fig. 11(a). From the high resolution transmission electron microscope (HR-TEM) image (Fig. 11(d)) and the selected area electron diffraction (SAED) image (Fig. 11(e)), it

could be seen that the angle between the $(1\,10\,1)$ plane, and the $(01\,\overline{1}0)$ plane was approximately 64°. This indicates that the twin belongs to a type of $\{10\,\overline{1}1\}$ twin [25]. The BF image in Fig. 11(b) showed typical dislocation features, demonstrating an influence of the internal stress on rapid cooling. The generation of dislocations in the Zr-2.5Nb

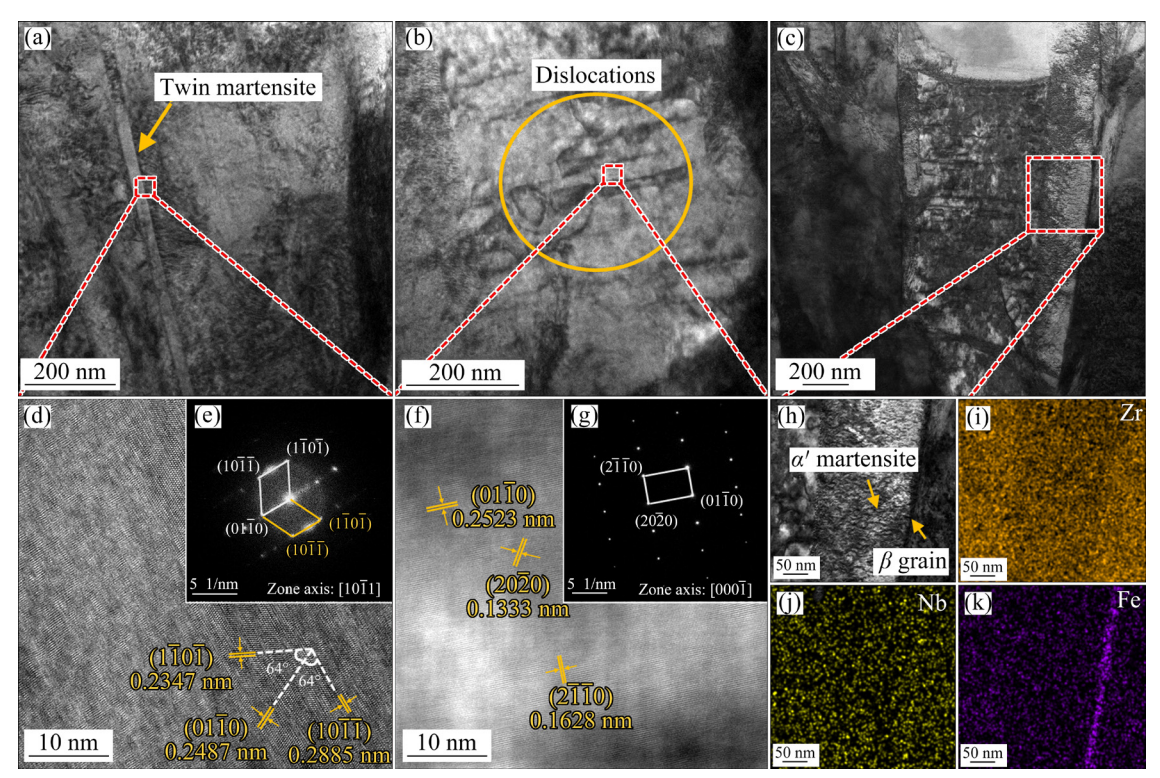


Fig. 11 TEM results of Zr–2.5Nb alloy prepared by LPBF at laser power of 160 W: (a–c, h) BF images showing twin martensite, dislocations, and martensite features; (d–g) HR-TEM images with an inverse fast-Fourier-transform (FFT) and SAED patterns; (i–k) EDS mapping result of Zr, Nb, and Fe in (h)

alloy during the LPBF process can be associated with thermal stresses caused by rapid melting/ cooling. Additionally, the presence of dislocations is influenced by the crystal structures of both the α phase and the β phase. Generally, the α phase has higher hardness and a lower coefficient of the thermal expansion compared to the β phase, and during heating/cooling the extrusion between the α and β phases occurs due to grain growth, resulting in the formation of dislocations between the two phases [26]. From the lattice image (Fig. 11(f)) and the SAED image (Fig. 11(g)) corresponding to the red box in Fig. 11(b), it could be observed that the zone axis was $[000\overline{1}]$ and the lattice spacing of the $(01\overline{10})$ plane, $(20\overline{20})$ plane, and $(2\overline{1}\overline{10})$ plane were measured to be 0.2523, 0.1333, and 0.1628 nm, respectively. These correspond to the martensitic α' phase. Figures 11(h-k) represent the distribution of the Zr, Nb, and Fe elements in the region corresponding to the red box in Fig. 11(c). The Zr and Nb elements exhibited a uniform distribution, while there was an enrichment of the Fe element at the boundaries of the β phase because the Fe element is a β -eutectoid alloying element [27]. In the Zr–Nb system, the Fe element primarily exists in the interphase regions and grain boundaries [28]. Fe can enrich in the metastable β -Zr phase before the β -Zr phase completely transformed into the β -Nb phase.

3.3 Microhardness and tensile properties

Figure 12 shows the microhardness variation of the Zr-2.5Nb alloy prepared with different laser powers and scanning speeds. The microhardness of the Zr-2.5Nb alloy ranged approximately from HV 260 to HV 280. The highest value of HV 280.74 was attained with a laser power of 160 W and a scanning speed of 1400 mm/s. By comparing Figs. 3 and 12, one could see that the variation in microhardness was generally positively correlated with the change in relative density. This indicated that the defects inside the material had a certain impact on microhardness, and the pores inside the material would collapse under load. At a scanning speed of 1400 mm/s, with changing the laser power from 120 to 180 W, the average microhardness increased from HV 269.59 HV 280.74 and then decreased to HV 278.78.

Figure 13 shows the tensile properties of the Zr-2.5Nb alloy samples prepared with different

laser powers at a scanning speed of 1400 mm/s and room temperature. The strain-stress curves are shown in Fig. 13(a), the tensile properties are shown in Fig. 13(b), and the mechanical properties are given in Table 3. As observed from the stress-strain curves, the Zr-2.5Nb alloy displayed a linear elastic deformation, followed by plastic deformation, without significant work hardening. Different laser powers influenced strongly the tensile properties, as shown in Fig. 13(b). With increasing the laser power, the ultimate tensile strength of the specimens showed a decreasing

trend, while the fracture elongation exhibited an initial increase followed by a decrease. At the laser power of 120 W, the ultimate tensile strength of the alloy was 979.63 MPa, and the minimal fracture elongation was 6.77%. At the laser power of 160 W, the maximal fracture elongation was 14.18%. However, if the laser power was increased to 180 W, it led to decreasing both the strength and elongation of the Zr–2.5Nb alloy.

Figure 14 presents the typical fracture morphology of the Zr–2.5Nb alloy prepared at different laser powers. At lower laser power, the

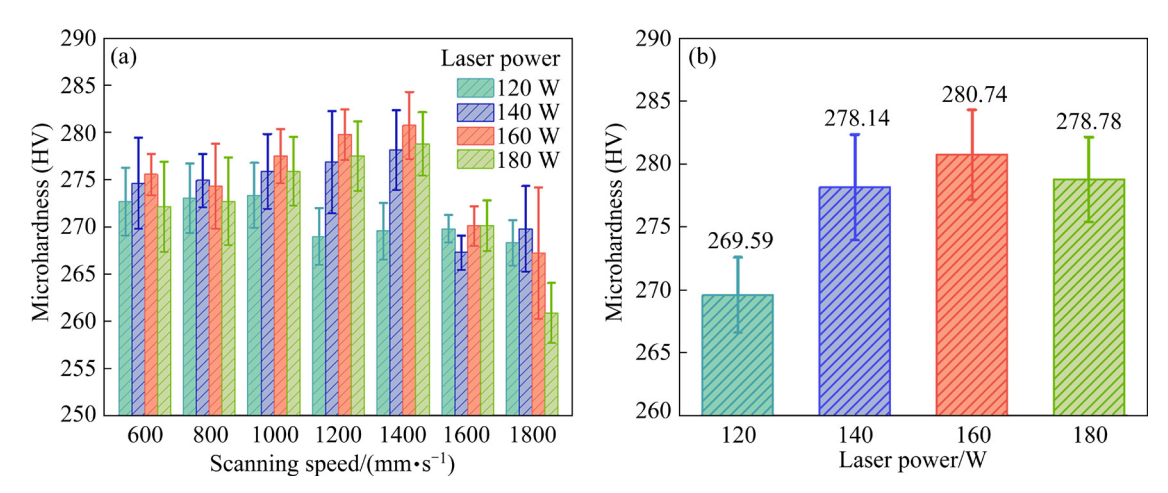


Fig. 12 Microhardness of Zr–2.5Nb alloy prepared by LPBF: (a) Histogram of microhardness variation with laser power and scanning speed; (b) Microhardness with different laser powers at scanning speed of 1400 mm/s

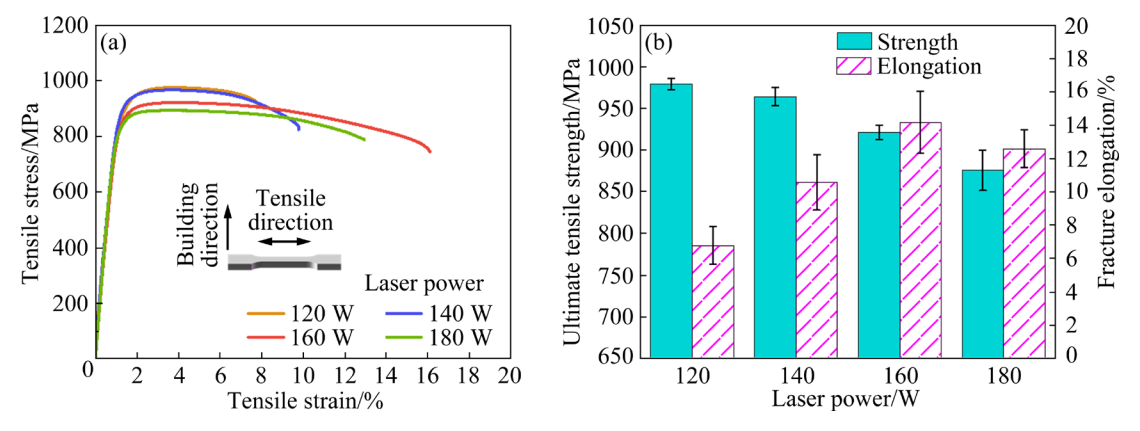


Fig. 13 Tensile properties of Zr-2.5Nb alloy prepared at different laser powers: (a) Strain-stress curves; (b) Ultimate tensile strength and fracture elongation

Table 3 Mechanical properties of Zr-2.5Nb alloy prepared at different laser powers

	1 1	- /1 1	1		
Laser	Yield	Tensile	Elementian/0/	Young's	Vickers
power/W	strength/MPa	strength/MPa	Elongation/%	modulus/GPa	hardness (HV)
120	851.00 ± 7.11	979.63±7.18	6.77 ± 1.13	83.11 ± 2.13	269.59±2.99
140	852.66 ± 17.08	964.25 ± 10.82	10.57 ± 1.66	86.58 ± 1.64	278.14 ± 4.79
160	822.14±4.18	921.44±8.64	14.18 ± 1.87	83.72 ± 2.84	280.74 ± 3.36
180	781.38 ± 15.85	875.92±24.12	12.59±1.13	87.33 ± 3.37	278.78±3.36

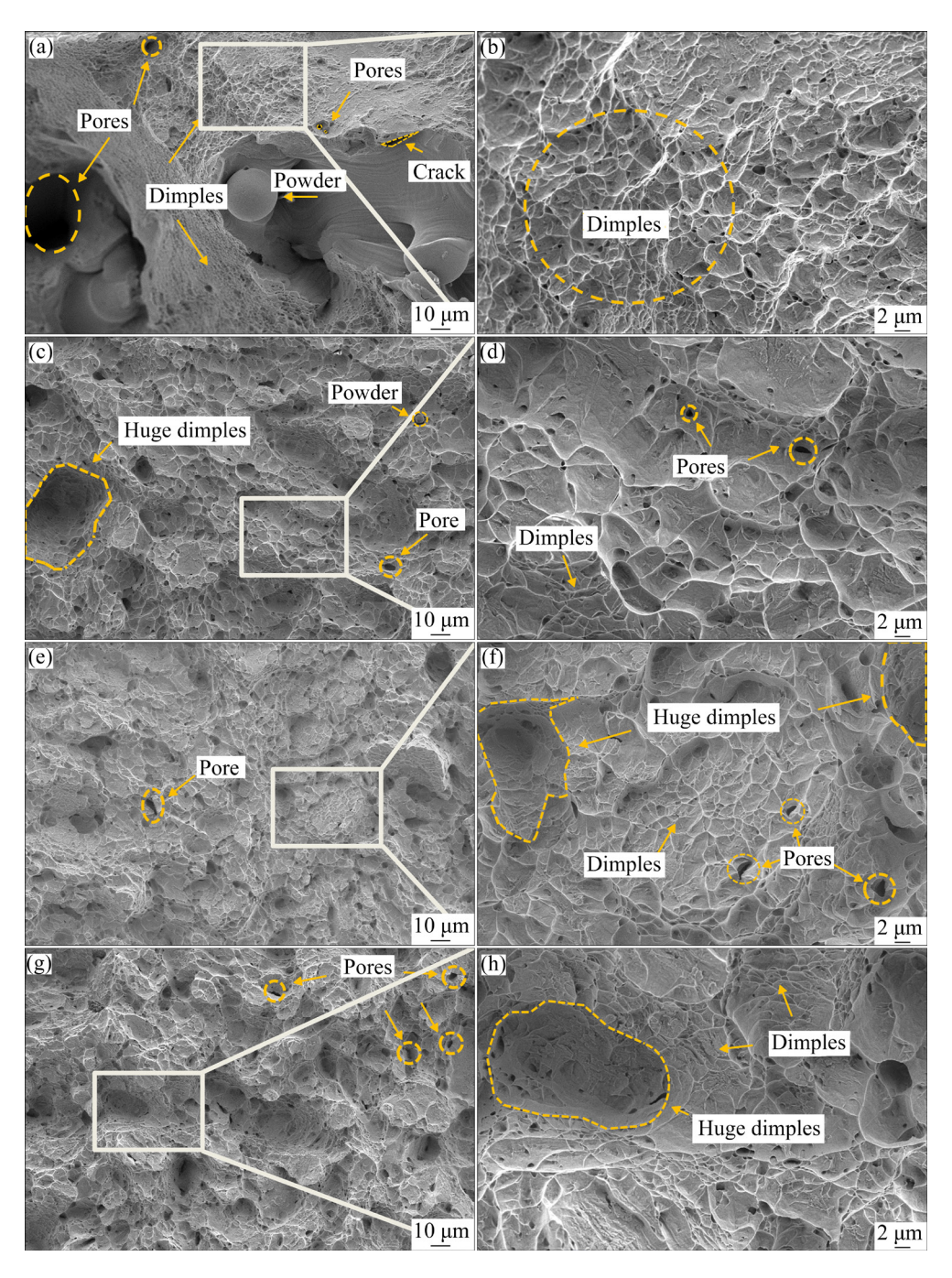


Fig. 14 Typical fracture morphologies of Zr–2.5Nb alloy prepared at different laser powers: (a, b) 120 W; (c, d) 140 W; (e, f) 160 W; (g, h) 180 W

fracture morphology exhibited clear evidence of large unfused spherical powder particles and pores, as depicted in Fig. 14(a). In the fracture morphology of the Zr–2.5Nb alloy tensile specimens prepared at the laser power of 120 W, cleavage steps were found to dominate. However, under high magnification, small dimples were locally observed, as demonstrated in Fig. 14(b). With increasing the laser power, the unfused

powder disappeared, and the dimples gradually increased. Huge dimples were consistently observed in all the fracture morphology of the Zr–2.5Nb alloy prepared at the laser power of 140–180 W (Figs. 14(c–h)), which indicated that the specimens had good ductility and localized plastic deformation under the tensile stress. Overall, the fracture pattern of the Zr–2.5Nb alloy exhibited a combination of quasi-cleavage and toughness

fracture. Additionally, microscopic pores were observed on all fracture surfaces of specimens. The findings implied that the process parameter window for LPBF Zr-2.5Nb alloy required further optimization.

The destructive strain and the ultimate tensile strength of the specimens were mainly influenced by the porosity and microstructural characteristics [29,30]. At a scanning speed of 1400 mm/s, the elongation initially increased and then decreased with the increase of the laser power, which was consistent with the change in relative density. With increasing the energy density, the width and depth of the melt pool also increased, which meant that the melt pool could extend beyond the current layer, enhancing interlayer bonding and obtaining excellent ductility. The samples undergoing action of proper laser energy could avoid insufficient fusion due to insufficient energy density and did not contain the keyholes due to excessive energy input.

Based on the EBSD results, it was found that increasing the laser power resulted in an increase in the volume fraction and grain size of the β phase and a stronger extrusion of the α and β phases, which further promoted dislocation motion. The volume fraction of low-angle grain boundaries (LAGBs) in sample prepared at laser power of 160 W (5.99%) was higher than that of 140 W (4.72%), which impeded the dislocation movement to some extent. However, if the laser power increased, the tensile strength of the Zr-2.5Nb alloy gradually decreased. This indicated that the dislocations caused by the compression of the α and β phases eventually prevailed.

Figure 15 illustrates the mechanical properties of currently reported Zr-Nb alloys [23,31-35] and pure Zr prepared by additive manufacturing [35]. It can be observed that the ultimate tensile strength of the Zr-2.5Nb alloy can approach approximately 1000 MPa, and the fracture elongation reaches 28%. In this study, the effect of the LPBF process parameters on the mechanical properties of the Zr-2.5Nb alloy was investigated for the first time. The tensile strength of the LPBF Zr-2.5Nb alloy can reach up to 975.6 MPa, which is the highest strength currently achieved for the Zr-2.5Nb alloys. In terms of ductility, the elongation of the Zr-2.5Nb alloy prepared in this study ranged from 6% to 16%, which was higher than that of pure Zr prepared by directed energy deposition (DED) [35] and slightly lower than that achieved through conventional processes such as cold rolling [34,35], hot rolling [23], and forging [31]. This is due to the fact that the fabrication of traditional Zr–Nb alloy components involves extensive thermo-mechanical treatments. For example, the fabrication of the Zr–Nb alloy pressure tubes involves the decomposition of ingots, extrusion, annealing, cold working, and other steps [31] and the synergistic processing of these various techniques has resulted in the excellent mechanical properties of the Zr–Nb alloys.

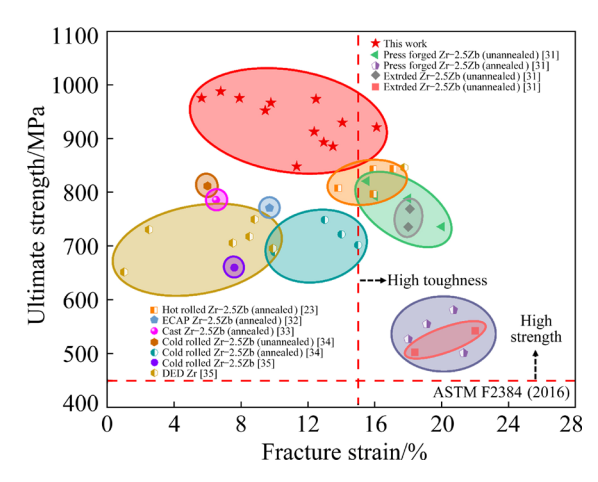


Fig. 15 Comparison of fracture strain and ultimate tensile strength of Zr–2.5Nb alloy prepared by LPBF with other reported Zr–Nb alloys [23,31–35] and additively manufactured pure Zr [35]

As well-known, the tensile strength in ASTM F2384 standard for wrought Zr-2.5Nb alloy for surgical implant is 450 MPa and the elongation is 15% under annealed conditions (red dashed line in Fig. 15). The LPBF Zr-2.5Nb alloy that has not undergone annealing treatment, possesses mechanical properties which are close to the standard ones. We note that the ductility of the Zr-2.5Nb alloy can be further improved after appropriate annealing treatment. Due to the advantages of LPBF technology in forming complex structures, this technology further expands the application range of the Zr-2.5Nb alloy, particularly in the field of personalized biomedical implants, where it holds significant application value.

3.4 Corrosion properties

Figure 16 presents EIS results after immersion in 3.5 wt.% NaCl solution for 1.5 h to reach the steady

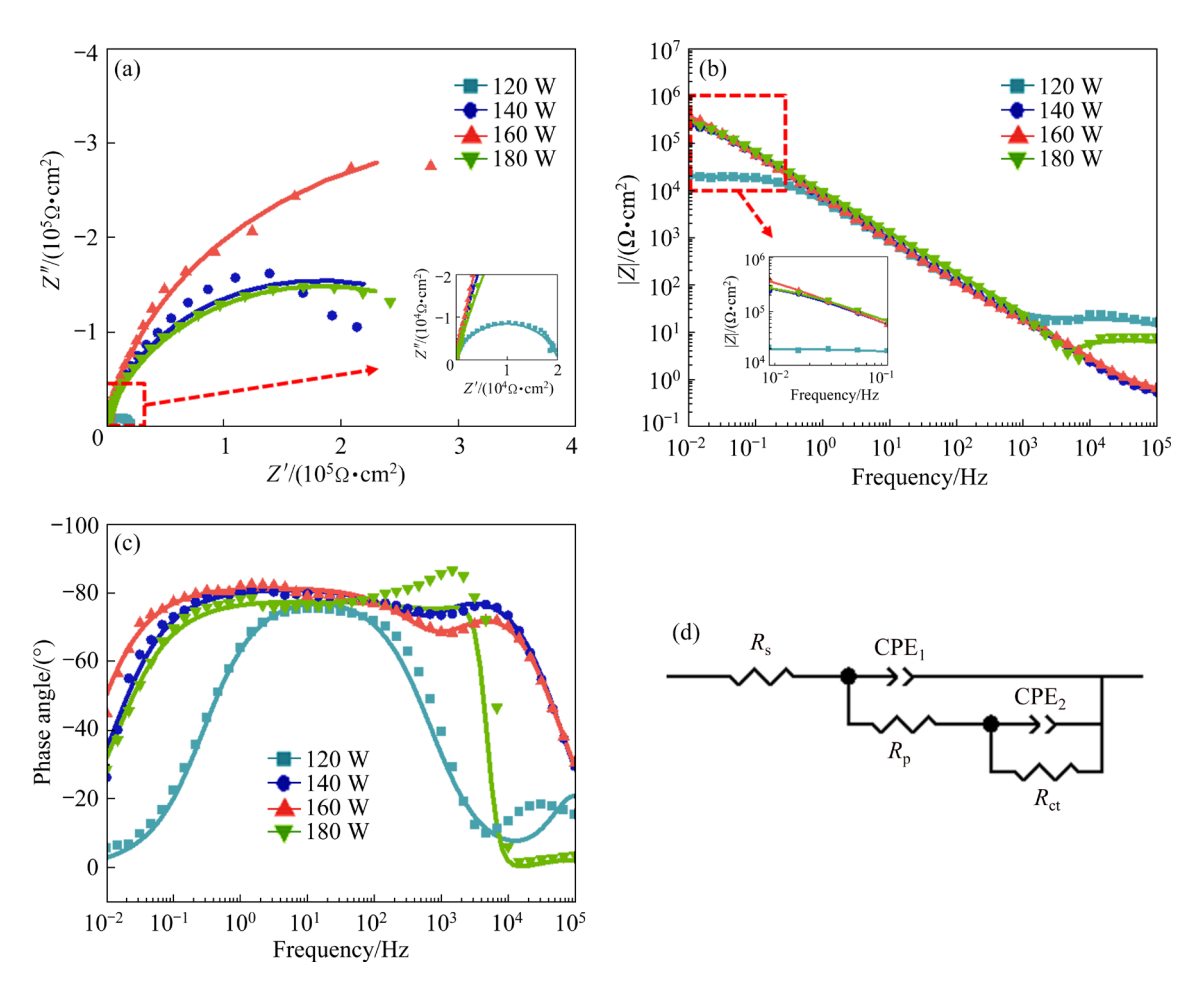


Fig. 16 EIS results of Zr–2.5Nb alloy samples prepared at different laser powers in 3.5 wt.% NaCl solution: (a) Nyquist plots; (b) Bode impedance magnitude plots; (c) Bode phase plots; (d) Corresponding equivalent circuit

state. In the Nyquist plots (Fig. 16(a)), the impedance spectra of the Zr–2.5Nb alloy prepared at the laser power of 120–180 W exhibited capacitive reactance arc characteristics. The radius of the capacitive reactance arc characterized the resistance, with a larger radius indicating higher surface resistance of the material and thus better corrosion resistance [36]. With increasing the laser power, the capacitive reactance arc showed a trend of first increasing and then decreasing, with the maximum radius of the capacitive reactance arc observed for the Zr–2.5Nb alloy prepared at the laser power 160 W. Similar trends were also observed in the Bode plot.

From the impedance magnitude plots (Fig. 16(b)), it can be observed that at the laser powers of 140 and 160 W, the Bode impedance magnitude curves of the Zr–2.5Nb alloy appeared smooth with consistent slopes, indicating that the oxide film was uniform and experienced uniform corrosion. In the mid-frequency region $(10^{3}-10^{-1}\,\mathrm{Hz})$, the impedance amplitude of Zr–2.5Nb

alloy prepared at all powers showed a linear relationship with the test frequency, displaying a slope near -1, demonstrating prominent capacitive resistance characteristics. Based on the corresponding resistive response at the solution/substrate interface [37], zooming in on the amplitude plots in the low-frequency region $(10^{-1}-10^{-2} \text{ Hz})$, it can be found that Zr-2.5Nb alloy prepared at laser power of 160 W exhibited significantly larger |Z| values, indicating a higher corrosion resistance.

The Bode phase plot is shown in Fig. 16(c), from which two peaks could be seen, indicating two-times constants in the equivalent circuit. The phase angle plot exhibited a capacitive response at phase angle of about -80° in the mid-frequency range. This indicated the existence of a typical passive film on the surface [38].

The electrochemical impedance spectrum was fitted using Zview software, and the corresponding equivalent circuit is illustrated in Fig. 16(d). In the

circuit, R_s represented the solution resistance, R_p represented the membrane layer resistance, R_{ct} represented the charge transfer resistance, and CPE was the constant phase element. The expression for the constant phase element impedance (Z_{CEP}) is written in Eq. (2) [39]:

$$Z_{\text{CEP}} = [Q(j\omega)^n]^{-1} \tag{2}$$

where Q is the constant phase coefficient, $j=\sqrt{-1}$, ω is the angular frequency, and n is the dispersion index (0 < n < 1). n value is related to the surface inhomogeneity. if n=1, the impedance is pure capacitance; if n=0, the impedance corresponds to pure resistance.

The fitted EIS data are shown in Table 4, where χ^2 is used to evaluate the reliability of the equivalent circuit fitting data. The magnitude of χ^2 was in the order of 10^{-3} – 10^{-2} , which indicated that the experimental data and fitted data were in good agreement. The Zr-2.5Nb alloy prepared at the laser power of 40 W exhibited a higher R_p value of $80.80 \Omega \cdot \text{cm}^2$, indicating its excellent ability to block the passage of ionic current. On the contrary, the Zr-2.5Nb alloys prepared at the laser power of 120 and 180 W had a poor ability to block the passage of ionic current. The charge transfer resistance (R_{ct}) plays a significant role in assessing the corrosion resistance of the passive film formed on the surface of the alloy. The higher the R_{ct} , the stronger the ability of the surface passive film to block the corrosive medium and the better the corrosion resistance of the alloy [40]. The R_{ct} value of the Zr-2.5Nb alloy first increased and then decreased with increasing laser power, and the Zr-2.5Nb alloy prepared at the laser power of 160 W had the highest R_{ct} value, measuring $6.96 \times 10^5 \,\Omega \cdot \text{cm}^2$, indicating the best corrosion resistance.

Dynamic potential polarization curves of the Zr-2.5Nb alloy prepared at different laser powers measured in 3.5 wt.% NaCl solution are illustrated in Fig. 17. As the applied potential was increased

from $-1.0 \,\mathrm{V}$ to the corrosion potential, a homogeneous cathodic response was observed in all tested samples. As the potential increased, a concurrent decrease of current density was observed. In the anodic region of the polarization curves, all samples spontaneously entered the passivation region as the potential increased. This result suggested that the alloy possessed a strong passivation ability and could form a stable passive film. It was evident that if the potential increased to a certain point, then the current density abruptly increased, indicating pitting corrosion occurred on the sample at that potential. Pitting corrosion of the Zr-2.5Nb alloy prepared at laser powers of 120 and 140 W occurred at approximately 0.5 V, while for the alloy prepared at laser powers of 160 and 180 W, the pitting corrosion occurred at around 0.25 V.

The corrosion potential (φ_{corr}) and corrosion current density (J_{corr}) of the Zr–2.5Nb alloy in 3.5 wt.% NaCl solution were obtained from Fig. 17 using the Tafel extrapolation method, and the values are given in Table 5. In general, the higher the value of φ_{corr} , the less likely the alloy will corrode, and the lower the value of J_{corr} , the lower the corrosion rate of the alloy [41]. By comparing the φ_{corr} and J_{corr} values of the Zr–2.5Nb alloy prepared at different laser powers, the φ_{corr} value was the highest at the laser power of 160 W, while the J_{corr} value was the smallest at the laser power of 180 W. Considering the impedance results, it can be concluded that the Zr–2.5Nb alloy prepared at the laser power of 160 W exhibited better corrosion resistance.

The results of electrochemical corrosion tests indicated that the Zr–2.5Nb alloy prepared at a suitable laser power can obtain superior corrosion resistance. The Zr–2.5Nb alloy prepared at the laser power of 160 W showed more excellent corrosion resistance in 3.5 wt.% NaCl solution. This was due to the presence of clusters of unfused powder and pores in the Zr–2.5Nb alloy samples prepared at too low or too high laser power. The presence of pores increased the contact area between the samples and

Table 4 EIS fitting data of Zr-2.5Nb alloy samples prepared at different laser powers

	0	<i>J</i> 1	1 1		1			
Laser power/W	$R_{\rm s}/(\Omega\cdot{\rm cm}^2)$	$CPE_1/(S \cdot s^n \cdot cm^{-2})$	n_1	$R_{\rm p}/(\Omega\cdot{\rm cm}^2)$	$CPE_2/(S \cdot s^n \cdot cm^{-2})$	n_2	$R_{\rm ct}/(\Omega\cdot{\rm cm}^2)$	χ^2
120	10.29	3.84×10^{-8}	0.9896	8.36	3.00×10^{-5}	0.8910	2.00×10 ⁵	2.38×10 ⁻²
140	0.45	6.26×10^{-6}	0.9431	80.80	1.29×10^{-5}	0.8540	3.65×10^{5}	3.54×10^{-3}
160	0.52	5.16×10^{-6}	0.9276	44.16	1.32×10^{-5}	0.8846	6.96×10^{5}	1.55×10^{-3}
180	6.19	3.63×10^{-6}	0.8649	0.59	3.07×10^{-10}	0.8339	3.69×10^{5}	8.55×10^{-2}

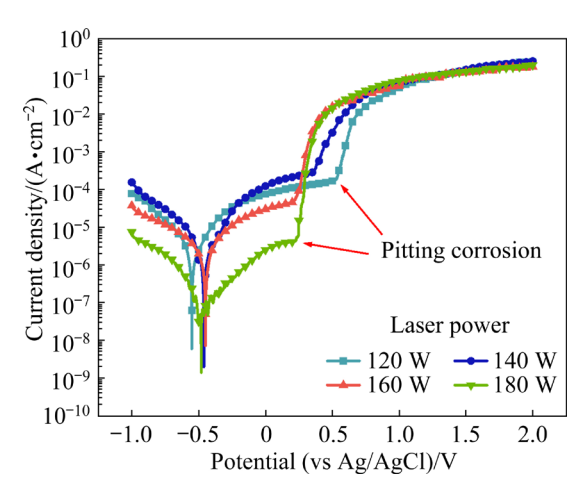


Fig. 17 Dynamic potential polarization curves of Zr–2.5Nb alloy samples prepared at different laser powers in 3.5 wt.% NaCl solution

 Table 5
 Corrosion results obtained from dynamic

 potential polarization curves

Laser power/W	$\varphi_{\rm corr}$ (vs Ag/AgCl)/V	$J_{ m corr}/({ m A\cdot cm^{-2}})$		
120	-0.551	2.05×10^{-6}		
140	-0.461	1.66×10^{-6}		
160	-0.449	1.83×10^{-6}		
180	-0.481	2.96×10^{-7}		

the NaCl solution, creating conditions for localized corrosion initiation, which subsequently resulted in strong pitting corrosion, while the oxide layer on the clusters of unfused powder weakened the corrosion resistance of the Zr–2.5Nb alloy [42].

Pitting corrosion in passive metals is thought to be caused by passivation breakdown [43]. Passivation breakdown is mainly categorized into the following three mechanisms: (1) the penetration mechanism, (2) the film-breaking mechanism, and (3) the adsorption mechanism [43,44]. Regardless of the mechanism, it is the Cl⁻ ions in the 3.5 wt.% NaCl solution that play a major role in the pitting process. The grain boundary region is usually a favorable location for Cl- ion adsorption, which leads to preferential corrosion at grain boundaries and an accelerated corrosion rate due to the enrichment of Cl⁻ ions, and the passive film is usually highly distorted at these positions, leading to passivation breakdown [45,46]. As shown in Fig. 18(a), the Zr-2.5Nb alloy is mainly composed of α/α' and β phases, and grain boundary between two phases may be a typical favorable location for the adsorption of Cl⁻ ions. JI et al [46] investigated the as-cast Ti–Zr alloys and found that corrosion pits are more likely to be produced in the region of the dense α -grain boundaries. This is because Clions are more easily enriched in the dense α -grain boundary region, resulting in a larger driving force for the diffusion of cation vacancies in the passive film near this region. The migration speed of cation vacancies is accelerated, leading to the destruction of the passive film and the formation of pits near the dense α -grain boundary region. When the number of cation vacancies reaches a critical level, it will cause breakdown of the passive film. Schematic diagrams are shown in Figs. 18(b, c).

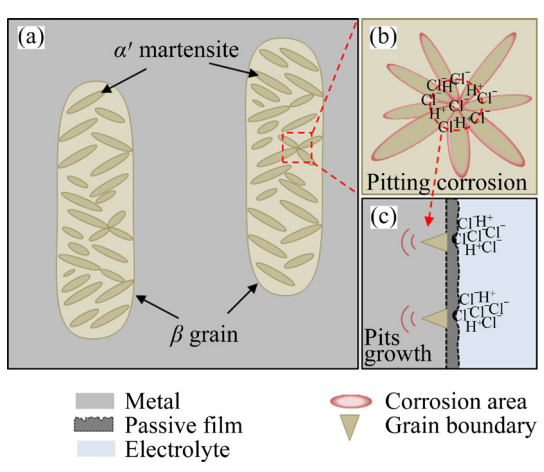


Fig. 18 Schematic illustration showing pitting corrosion principle of Zr–2.5Nb alloy: (a) Schematic illustration of microstructure; (b) Grain boundary region enriched with Cl⁻ ions; (c) Destruction of passive film and formation of craters in vicinity of grain boundaries

4 Conclusions

- (1) The density of the LPBF Zr–2.5Nb alloy was affected by the laser power and scanning speed. Nearly fully dense Zr–2.5Nb alloy could be obtained at laser power of 160 W, and scanning speed of 1400 mm/s with no obvious pores in the surface morphology.
- (2) Acicular-shaped martensitic phases were present inside the columnar original β grains growing along the Zr-2.5Nb alloy building direction. With increasing the laser power, the transition of $\alpha' \rightarrow \alpha + \beta$ was accelerated and the amount of β phase gradually increased.
- (3) The variation of elongation and tensile strength was mainly affected by porosity and microstructure. A tensile strength of 979.63 MPa was obtained at the laser power of 120 W, which is

the maximal strength currently available in the research field of the Zr-2.5Nb alloy.

(4) The Zr-2.5Nb alloy could spontaneously form passive film in 3.5 wt.% NaCl solution. The appropriate laser power could result in a more uniform passive film, enhancing the corrosion resistance of the Zr-2.5Nb alloy. Lower or higher laser power would lead to the generation of unfused powder and pores, affecting the corrosion resistance.

CRediT authorship contribution statement

Yun-lei HUANG: Data curation, Formal analysis, Investigation, Methodology, Visualization, Writing -Original draft, Validation, Writing - Review & editing; Vyacheslav **TROFIMOV:** Conceptualization, Methodology, Supervision, Writing – Review & editing; Feng LIU: Funding acquisition, Investigation; Ming YAN: Conceptualization, **Funding** acquisition, Supervision, Writing - Review & editing; Jie ZHAN: acquisition, Investigation; Hui-xia Methodology, Project administration, Resources; Da **ZENG:** Methodology, Project administration, Resources; Yong-qiang YANG: Conceptualization, Methodology, Supervision; Chang-hui SONG: Conceptualization, Formal analysis, Funding acquisition, Investigation, Methodology, Supervision, Writing – Review & editing.

Declaration of competing interest

The authors declare that they have no known competing financial interests or personal relationships that could have appeared to influence the work reported in this paper.

Acknowledgments

This work was supported by the National Key Area Research and Development Program of China (No. 2023YFB4606702), Guangdong Basic and Applied Basic Research Foundation, China (No. 2022B1515120066), Dongguan Key Area Research and Development Program, China (No. 20221200300182), the National Natural Science Foundation of China (No. 52271032), and Key Research and Development Program of Jiangsu Province, China (No. K22251901).

References

[1] HAROONI A, NASIRI A M, GERLICH A P, KHAJEPOUR A, KHALIFA A, KING J M. Processing window development for laser cladding of zirconium on zirconium alloy [J]. Journal of Materials Processing Technology, 2016,

- 230: 263-271.
- [2] DING Yu-miao, LIU Shu-guang, XIA Chao-qun, ZOU Xian-rui, LIU Di, WANG Yanqing, YANG Tai, LI Qiang. Thermal oxidation of novel Zr-Ti-Al-V alloy with high strength and toughness and its influence on the corrosion behavior [J]. Surface and Coatings Technology, 2021, 423: 127576.
- [3] WANG Cai-xu, ZHAO Xiao-li, LI Shu-jun, LIU Lu, ZHANG De-liang, NIINOMI M. Low-cost surface modification of a biomedical Zr-2.5Nb alloy fabricated by electron beam melting [J]. Journal of Materials Science & Technology, 2023, 143: 178-188.
- [4] TULI V, BURR P, CLAISSE A, CAZORLA C. Thermodynamic stability of *β*-phases in Zr–Nb alloys [J]. Physical Review Materials, 2023, 7(11): 113607.
- [5] CHAI Lin-jiang, CHEN Ke, WANG Shu-yan, XIA Ji-ying, WANG Ting-ting, YANG Zhi-nan. Microstructural characteristics of as-forged and β-air-cooled Zr–2.5Nb alloy [J]. Transactions of Nonferrous Metals Society of China, 2018, 28(7): 1321–1328.
- [6] SONG Tian-shuo, LIU Shu-guang, CHEN Bo-han, CUI Zi-yao, ZOU Xian-rui, ZHANG Shi-liang, LI Qiang, XIA Chao-qun. Enhanced corrosion and wear resistance via thermal oxidation treatment on Zr-2.5Nb alloy for implant applications [J]. Surface and Coatings Technology, 2023, 458: 129365.
- [7] ZINKLE S J, WAS G S. Materials challenges in nuclear energy [J]. Acta Materialia, 2013, 61: 735–758.
- [8] XIAO Yun-mian, YANG Yong-qiang, WANG Di, LIU Lin-qing, LIU Zi-bin, WU Shi-biao, ZHOU Han-xiang, LIU Zi-xin, SONG Chang-hui. In-situ synthesis of high strength and toughness TiN/Ti6Al4V sandwich composites by laser powder bed fusion under a nitrogen-containing atmosphere [J]. Composites Part B: Engineering, 2023, 253: 110534.
- [9] XIAO Yun-mian, YANG Yong-qiang, WANG Di, ZHOU Han-xiang, LIU Zi-bin, LIU Lin-qing, WU Shi-biao, SONG Chang-hui. In-situ synthesis of spatial heterostructure Ti composites by laser powder bed fusion to overcome the strength and plasticity trade-off [J]. International Journal of Machine Tools and Manufacture, 2024, 196: 104117.
- [10] SONG Chang-hui, LIU Li-sha, DENG Zheng-tai, LEI Hao-yang, YUAN Fu-zhen, YANG Yong-qiang, LI Yue-yue, YU Jia-kuo. Research progress on the design and performance of porous titanium alloy bone implants [J]. Journal of Materials Research and Technology, 2023, 23: 2626–2641.
- [11] XIAO Yun-mian, SONG Chang-hui, LIU Zi-bin, LIU Lin-qing, ZHOU Han-xiang, WANG Di, YANG Yong-qiang. In-situ additive manufacturing of high strength yet ductility titanium composites with gradient layered structure using N₂ [J]. International Journal of Extreme Manufacturing, 2024, 6(3): 35001.
- [12] SAHASRABUDHE H, BANDYOPADHYAY A. Laser-based additive manufacturing of zirconium [J]. Applied Sciences, 2018, 8(3): 393.
- [13] SONG Chang-hui, ZOU Zhuang, YAN Zhong-wei, YAO Xi-yu, LIU Feng, YANG Yong-qiang, YAN Ming, HAN Chang-jun. Microstructural and mechanical property evolution of a nuclear zirconium-4 alloy fabricated via laser

- powder bed fusion and annealing heat treatment [J]. Virtual and Physical Prototyping, 2023, 18(1): e2189597.
- [14] YUE Mei-feng, LIU Ying, HE Gong-ming, LIAN Li-xian. Microstructure and mechanical performance of zirconium, manufactured by selective laser melting [J]. Materials Science and Engineering A, 2022, 840: 142900.
- [15] AN Na-ying, SHUAI San-san, CHEN Chao-yue, LEI Li-ming, WANG Jiang, REN Zhong-ming. Quantitative study of geometric characteristics and formation mechanism of porosity defects in selective laser melted Ti6Al4V alloy by micro-computed tomography [J]. Transactions of Nonferrous Metals Society of China, 2023, 33(10): 2986–3002.
- [16] KING W E, BARTH H D, CASTILLO V M, GALLEGOS G F, GIBBS J W, HAHN D E, KAMATH C, RUBENCHIK A M. Observation of keyhole-mode laser melting in laser powder-bed fusion additive manufacturing [J]. Journal of Materials Processing Technology, 2014, 214(12): 2915– 2925.
- [17] BAYAT M, THANKI A, MOHANTY S, WITVROUW A, YANG Shou-feng, THORBORG J, TIEDJE N, HATTEL J. Keyhole-induced porosities in laser-based powder bed fusion (L-PBF) of Ti6Al4V: High-fidelity modelling and experimental validation [J]. Additive Manufacturing, 2019, 30: 100835.
- [18] MARTIN A A, CALTA N P, HAMMONS J A, KHAIRALLAH S A, NIELSEN M H, SHUTTLESWORTH R M, SINCLAIR N, MATTHEWS M J, JEFFRIES J R, WILLEY T M, LEE J R I. Ultrafast dynamics of laser-metal interactions in additive manufacturing alloys captured by in situ X-ray imaging [J]. Materials Today Advances, 2019, 1: 100002.
- [19] LIU Hui, YU Han-yang, GUO Chuan, CHEN Xu-liang, ZHONG Shi-yu, ZHOU Lin, OSMAN A, LU Jian. Review on fatigue of additive manufactured metallic alloys: Microstructure, performance, enhancement, and assessment methods [J]. Advanced Materials, 2023, 36(17): 2306570.
- [20] DAYMOND M R, HOLT R A, CAI S, MOSBRUCKER P, VOGEL S C. Texture inheritance and variant selection through an hcp-bcc-hcp phase transformation [J]. Acta Materialia, 2010, 58: 4053–4066.
- [21] CHAI Lin-jiang, CHEN Bao-feng, WANG Shu-yan, ZHANG Zhuo, MURTY K L. Microstructural, textural and hardness evolution of commercially pure Zr surface-treated by high current pulsed electron beam [J]. Applied Surface Science, 2016, 390: 430–434.
- [22] QIU Chun-lei, ADKINS N J E, ATTALLAH M M. Microstructure and tensile properties of selectively laser-melted and of HIPed laser-melted Ti-6Al-4V [J]. Materials Science and Engineering A, 2013, 578: 230-239.
- [23] LIU S Y, ZHANG J Y, KUANG J, BAO X Y, ZHANG D D, ZHANG C L, YANG J K, LIU G, SUN J. Designing hetero-structured ultra-strong and ductile Zr-2.5Nb alloys: Utilizing the grain size-dependent martensite transformation during quenching [J]. Journal of Materials Science & Technology, 2022, 125: 198-211.
- [24] CHAI L J, LUAN B F, GAO S S, CHEN J W, LIU Q. Study of precipitate evolution and recrystallization of β-quenched Zr–Sn–Nb–Fe–Cr–Cu alloy during aging [J]. Journal of

- Nuclear Materials, 2012, 427(1/2/3): 274-281.
- [25] CHAI Lin-jiang, CHEN Bao-feng, ZHOU Zhi-ming, MURTY K L, MA Yan-long, HUANG Wei-jiu. A special twin relationship or a common Burgers misorientation between α plates after β quenching in Zr alloy? [J]. Materials Characterization, 2015, 104: 61–65.
- [26] LIU Yang, PANG Zhi-cong, LI Ming, WANG Yong-gang, WANG Di, SONG Chang-hui, LI Shu-xin. Investigation into the dynamic mechanical properties of selective laser melted Ti-6Al-4V alloy at high strain rate tensile loading [J]. Materials Science and Engineering A, 2019, 745: 440-449.
- [27] ZHAO Ping-ping, SONG Ying-wei, DONG Kai-hui, SHAN Da-yong, HAN En-hou. Corrosion behavior of dual-phase Ti-6Al-4V alloys: A discussion on the impact of Fe content [J]. Journal of Alloys and Compounds, 2021, 858: 157708.
- [28] HARTE A, GRIFFITHS M, PREUSS M. The characterisation of second phases in the Zr–Nb and Zr–Nb–Sn–Fe alloys: A critical review [J]. Journal of Nuclear Materials, 2018, 505: 227–239.
- [29] SALARIAN M, ASGARI H, VLASEA M. Pore space characteristics and corresponding effect on tensile properties of Inconel 625 fabricated via laser powder bed fusion [J]. Materials Science and Engineering A, 2020, 769: 138525.
- [30] GU Dong-dong, GUO Meng, ZHANG Hong-mei, SUN Yi-xuan, WANG Rui, ZHANG Lei. Effects of laser scanning strategies on selective laser melting of pure tungsten [J]. International Journal of Extreme Manufacturing, 2020, 2(2): 025001.
- [31] SAIBABA N, VAIBHAW K, NEOGY S, MANI KRISHNA K V, JHA S K, PHANI BABU C, RAMANA RAO S V, SRIVASTAVA D, DEY G K. Study of microstructure, texture and mechanical properties of Zr–2.5Nb alloy pressure tubes fabricated with different processing routes [J]. Journal of Nuclear Materials, 2013, 440(1/2/3): 319–331.
- [32] TERENTYEV V F, DOBATKIN S V, NIKULIN S A, KOPYLOV V I, PROSVIRNIN D V, ROGACHEV S O, BANNYKH I O. Fatigue strength of submicrocrystalline Ti and Zr–2.5%Nb alloy after equal channel angular pressing [J]. Kovove Mater, 2011, 49(1): 65–73.
- [33] KONDO R, NOMURA N, SUYALATU, TSUTSUMI Y, DOI H, HANAWA T. Microstructure and mechanical properties of as-cast Zr–Nb alloys [J]. Acta Biomaterialia, 2011, 7(12): 4278–4284.
- [34] YANG Z N, ZHANG F C, LIU F C, YAN Z G, XIAO Y Y. Achieving high strength and toughness in a Zr–2.3Nb alloy by the formation of duplex microstructure [J]. Materials & Design, 2012, 40: 400–406.
- [35] HAROONI A, IRAVANI M, KHAJEPOUR A, KING J M, KHALIFA A, GERLICH A P. Mechanical properties and microstructures in zirconium deposited by injected powder laser additive manufacturing [J]. Additive Manufacturing, 2018, 22: 537–547.
- [36] SU Bao-xian, LUO Liang-shun, WANG Bin-bin, SU Yan-qing, WANG Liang, RITCHIE R O, GUO En-yu, LI Ting, YANG Hui-min, HUANG Hai-guang, GUO Jing-jie, FU Heng-zhi. Annealed microstructure dependent corrosion behavior of Ti-6Al-3Nb-2Zr-1Mo alloy [J]. Journal of Materials Science & Technology, 2021, 62: 234-248.
- [37] KONG Wei-cheng, YU Zhou, HU Jun. Electrochemical

- performance and corrosion mechanism of Cr–DLC coating on nitrided Ti6Al4V alloy by magnetron sputtering [J]. Diamond and Related Materials, 2021, 116: 108398.
- [38] ZHOU F Y, WANG B L, QIU K J, LIN W J, LI L, WANG Y B, NIE F L, ZHENG Y F. Microstructure, corrosion behavior and cytotoxicity of Zr–Nb alloys for biomedical application [J]. Materials Science and Engineering C, 2012, 32(4): 851–857.
- [39] YANG Liang, ZHANG Hao-ran, ZHANG Shan, SHI Zhi-lin, WEI Chao, MA Ming-zhen, LIU Ri-ping. Corrosion behavior of Ti-based bulk amorphous alloys in acidic solutions [J]. Transactions of Nonferrous Metals Society of China, 2024, 34(3): 874–889.
- [40] CAI Fei, ZHOU Qi, CHEN Jun-kai, ZHANG Shi-hong. Effect of inserting the Zr layers on the tribo-corrosion behavior of Zr/ZrN multilayer coatings on titanium alloys [J]. Corrosion Science, 2023, 213: 111002.
- [41] LIU Han-ze, YAN Zhi-cheng, CHEN Qi, ZHANG Hao, FENG Yu, QI Zhi-gang, WANG Zhao-xuan, PAN Shaopeng, JIA Yi-yong, WANG Wei-min. Enhancing corrosion resistance of Al50Ni50 alloy by increasing cooling rate plus annealing [J]. Transactions of Nonferrous Metals Society of China, 2024, 34(3): 769–785.

- [42] NIU Xiao-miao, SHEN Hong-yao, FU Jian-zhong, YAN Jin-wen, WANG Yu. Corrosion behaviour of laser powder bed fused bulk pure magnesium in hank's solution [J]. Corrosion Science, 2019, 157: 284–294.
- [43] XIA C Q, FENG Z H, YANG Y H, ZHANG Z G, JING R, PAN B, ZHANG X Y, MA M Z, LIU R P. Microstructure and corrosion behavior of the annealed Zr-40Ti-5Al-4V alloys [J]. Journal of Alloys and Compounds, 2016, 666: 301–308.
- [44] SOLTIS J. Passivity breakdown, pit initiation and propagation of pits in metallic materials Review [J]. Corrosion Science, 2015, 90: 5–22.
- [45] LI J, LI S J, HAO Y L, HUANG H H, BAI Y, HAO Y Q, GUO Z, XUE J Q, YANG R. Electrochemical and surface analyses of nanostructured Ti–24Nb–4Zr–8Sn alloys in simulated body solution [J]. Acta Biomaterialia, 2014, 10(6): 2866–2875.
- [46] JI Peng-fei, LIU Shu-guang, SHI Chun-bao, XU Kui-xue, WANG Zhen-guo, CHEN Bo-han, LI Bo, YANG Yu-jing, LIU Ri-ping. Synergistic effect of Zr addition and grain refinement on corrosion resistance and pitting corrosion behavior of single α-phase Ti–Zr-based alloys [J]. Journal of Alloys and Compounds, 2022, 896: 163013.

激光粉末床熔融制备 Zr-2.5Nb 合金的显微组织、 力学性能和腐蚀行为

黄云磊¹, Vyacheslav TROFIMOV¹, 刘 峰², 严 明 ^{3,4}, 詹 杰², 李会霞⁵, 曾 达⁶, 杨永强¹, 宋长辉¹

- 1. 华南理工大学 机械与汽车工程学院,广州 510641;
- 2. 中广核研究院有限公司 反应堆放废与放化研究所,深圳 518028;
 - 3. 南方科技大学 嘉兴研究院, 嘉兴 314031;
 - 4. 南方科技大学 第一附属医院 介入放射科,深圳 518020;
 - 5. 西安赛隆增材技术股份有限公司, 西安 710016;
 - 6. 大博医疗科技股份有限公司, 厦门 361026

摘 要: 对激光粉末床熔融制备 Zr-2.5Nb 合金的激光功率与扫描速度等工艺参数进行优化,并研究不同激光功率下成形的显微组织、力学性能和耐腐蚀性能。结果表明,获得了相对密度超过 99%、极限抗拉强度 980 MPa、断裂伸长率 14.18%的样品。当扫描速度为 1400 mm/s,激光功率从 120 W 增加至 180 W,Zr-2.5Nb 合金的微观结构主要发生 α '马氏体粗化和针状 α '马氏体转变为锯齿状这两个变化过程 (β - α '/ α - α + β),材料致密化和 α '马氏体组织转变对材料的延展性和耐腐蚀性能具有积极影响,但在低功率或高功率下,样品中的未熔颗粒和孔隙降低了材料的延展性和耐腐蚀性能,同时 β 相数量和尺寸的增加会促进位错运动,导致抗拉强度降低。不同激光功率下制备的样品电化学过程中均会自发形成钝化膜,在 160 W 激光功率下制备的 Zr-2.5Nb 合金具有最优的耐腐蚀性能。

关键词: Zr-2.5Nb 合金: 激光粉末床熔融; 显微组织: 力学性能: 耐腐蚀性能

(Edited by Bing YANG)